PHYSICAL REVIEW E **102**, 043306 (2020)

High-order kinetic flow solver based on the flux reconstruction framework

Ji Li,[*] Chengwen Zhong ,[†] and Sha Liu [‡]
National Key Laboratory of Science and Technology on Aerodynamic Design and Research, Northwestern Polytechnical University,
Xi'an, Shaanxi 710072, China

(Received 14 July 2020; accepted 17 September 2020; published 8 October 2020)

The goal of this paper is to develop a high-order numerical method based on the kinetic inviscid flux (KIF) method and flux reconstruction (FR) framework. The KIF aims to find a balance between the excellent merits of the gas-kinetic scheme (GKS) and the lower computational costs. The idea of KIF can be viewed as an inviscid-viscous splitting version of the gas-kinetic scheme, and Shu and Ohwada have made the fundamental contribution. The combination of totally thermalized transport (TTT) scheme and kinetic flux vector splitting (KFVS) method are achieved in KIF. Using a coefficient which is related to time step and averaged collision time, KIF can adjust the weights of TTT and KFVS flux in the simulation adaptively. By doing the inviscid-viscous splitting, KIF is very suitable and easy to integrate into the existing framework. The well-understood FR framework is used widely for the advantages of robustness, economical costs, and compactness. The combination of KIF and FR is originated by three motivations. The first purpose is to develop a high-order method based on the gas-kinetic theory. The second reason is to keep the advantages of GKS. The last aim is that the designed method should be more efficient. In present work, we use the KIF method to replace the Riemann flux solver applied in the interfaces of elements. The common solution at the interface is computed according to the gas-kinetic theory, which makes the combination of KIF and FR scheme more reasonable and available. The accuracy and performance of present method are validated by several numerical cases. The Taylor-Green vortex problem has been used to verify its potential to simulate turbulent flows.

DOI: 10.1103/PhysRevE.102.043306

I. INTRODUCTION

The gas-kinetic scheme (GKS) developed by Xu [1,2] is based on the idea of Bhatnagar *et al.* [3]. In recent years, GKS is on the way to become the preferred numerical method in the fluid dynamics. Compared with the traditional Navier-Stokes numerical method, GKS is of high spatial and temporal accuracy. The advantages of GKS have been recognized in the simulation of turbulent flows [4–8], shock-boundary interaction, hypersonic flows [2,9], and nonequilibrium simulations [10,11]. A series of studies based on the GKS has been conducted on the immersed boundary method [12–14], implicit temporal marching [15], and dual-time strategy [16] for unsteady flows.

In the field of computational fluid dynamics (CFD), a numerical algorithm can be classified as a low- or high-order method according to the numerical accuracy approached. For the features of robustness and economical costs, the low-order methods are still popular in the aeronautical industry. Compared with the low-order method, the high-order method is more accurate, which has the potential of providing more details of the flow fields [17,18]. However, using the high-order method in real industry is still a challenge, which has attracts the interest of many researchers from all over the world. The development of high-order GKS can be traced back to the study of Q. Li [19]. J. Luo [20], G. Zhou [21], L. Pan [22–24], X. Ji [25,26], and F. Zhao [27] have made great contributions to the high-order gas-kinetic scheme.

Although the high-order gas-kinetic scheme has been studied quite well, the development of the high-order gas-kinetic scheme has never stopped. In present work, we focus on the combination of the kinetic inviscid flux (KIF) and flux reconstruction (FR) methods. The combination of KIF and FR is originated by three motivations. The first purpose is to develop a high-order method based on the gas-kinetic theory. The second reason is to keep the advantages of GKS. The last aim is that the designed method should be more efficient. In order to find a balance between the advantages of the gas-kinetic scheme and lower computational costs, KIF was proposed by S. Liu [28]. The KIF scheme is a combination of the totally thermalized transport (TTT) scheme and the kinetic flux vector splitting method (KFVS). The TTT scheme, which does not introduce extra artificial viscosity in a smooth flow area, can approach the boundary layer accurately. TTT has a property similar to central schemes, so it also cannot capture the discontinuity properly. The KFVS is a shock capturing scheme with good robustness. The combination is a good idea, which means that we use the TTT scheme where the flow is smooth and the KFVS method where discontinuity exists. The kernel of the KIF method is to adjust the weights of the TTT and KFVS in the simulation automatically.

To develop a high-order kinetic flux solver, it is critical to adopt the advantages from the traditional high-order method based on the Navier-Stokes equation. Since the late 1990s, the high-order numerical method is one of the research hotspots

---

[*] leejearl@mail.nwpu.edu.cn

[†] Corresponding author: zhongcw@nwpu.edu.cn

[‡] shaliu@nwpu.edu.cn

in the field of CFD. Many of researchers have devoted their attention to such a challenge, and a large numbers of high-order numerical methods have been developed under the frameworks of the finite-volume method, finite-difference method, and finite-element method. Some of the schemes have notable features and have been used widely. For example, we have the k-exact method [29], essentially nonoscillatory (ENO) method [30–33], weighted ENO (WENO) method [34–36], discontinuous Galerkin (DG) method [37], radial basis function method [38], compact least-squares (CLS) reconstruction method [39,40], and variational reconstruction method [41]. An excellent review of the high-order methods is presented by Z. Wang [42].

The flux reconstruction method, first proposed by H. T. Huynh [43,44], aims to be more popular in both the research and real industry fields. The designed features of robustness, economical costs, and compactness make it well understood and available. A particular FR scheme depends on three factors [45], namely the distribution of solution points, the Riemann flux solver applied at the interfaces, and the choice of the correction functions $\mathcal{G}$ and $\mathcal{H}$. It has been proved that the flux reconstruction method can recover the simplified DG and staggered grid scheme with specific factors, and the conservation also has been proved in Ref. [43]. Based on the study of Jameson [46], a class of energy stable flux reconstruction method was proposed by Vincent, Castonguay, and Jameson (VCJH) [45]. The VCJH scheme was used for triangular elements [47]. Until now, the VCJH correct function has played an important role in the FR framework.

In the present work, the combination of KIF and FR is achieved by (a) replacing the Riemann solver applied on the interface of elements with KIF, (b) using the gas-kinetic theory to compute the common solution on the interface, and (c) implementing the inviscid-viscous splitting strategy in the simulation. The present paper is organized as follows. In Sec. II, the KIF method and the flux reconstruction framework are introduced. Several numerical tests are set up in Sec. III, and the numerical accuracy of the present method is validated. The last section of paper is a short conclusion.

II. NUMERICAL METHOD

The FR method, which takes advantage of DG and the staggered grid scheme [48,49], was first developed by H. T. Huynh [43,44]. It focuses on the features of robustness, economical costs, and compactness. The flux reconstruction method has attracted attention because it is well understood and widely available. In this section, the high-order kinetic flux solver based on the flux reconstruction framework will be introduced.

A. Governing equation

For a one-dimensional problem, the Bhatnagar-Gross-Krook (BGK) model [3] in the x direction is

$$f_t + u f_x = \frac{g-f}{\tau}, \tag{1}$$

where u is the particle velocity, f represents the gas distribution function, g denotes the equilibrium state approached by f, and τ is related to the averaged collision time. The equilibrium state is known as a Maxwellian distribution and reads as follows:

$$g = \rho\left(\frac{\lambda}{\pi}\right)^{\frac{K+1}{2}} e^{-[(u-U)^2+\xi^2]}, \tag{2}$$

where ρ is the density and U is the macroscopic velocity. λ, which reads as $\lambda = m/(2kT)$, is related to the temperature T of gas, m represents the molecular mass, and k denotes the Boltzmann constant. The total number of degrees of freedom K in ξ equals $(5-3\gamma)/(\gamma-1)+2$, γ is the ratio of specific heat, and $\boldsymbol{\xi}^2 = \sum_{i=1}^{K} \xi_i^2$.

According to the kinetic theory of gases, both the distribution function f and the equilibrium state g are functions of particle velocities u, space x, and time t. Taking the moments of distribution function f, the macroscopic conservative variable $\boldsymbol{w}$ can be obtained as follows:

$$\boldsymbol{w} = \begin{pmatrix} \rho \\ \rho U \\ E \end{pmatrix} = \int \boldsymbol{\psi} f d\Xi, \quad \boldsymbol{\psi} = \left(1, u, \frac{1}{2}(u^2+\boldsymbol{\xi}^2)\right)^T, \tag{3}$$

where $d\Xi = du(\prod_{i=1}^{K} d\xi_i)$. In order to obtain the spatial discretization in the flux reconstruction framework, we take moments of $\boldsymbol{\psi}$ in Eq. (1) and integrate it with $d\Xi$ in phase space,

$$\int (f_t + u f_x)\boldsymbol{\psi} d\Xi = -\int \frac{f-g}{\tau}\boldsymbol{\psi} d\Xi. \tag{4}$$

Using the compatibility condition

$$\int \frac{g-f}{\tau}\boldsymbol{\psi} d\Xi = 0, \tag{5}$$

we can get the following formula:

$$\boldsymbol{w}_t + \boldsymbol{G}_x = 0, \quad \boldsymbol{G} = \int u f \boldsymbol{\psi} \boldsymbol{d}\Xi, \tag{6}$$

where $\boldsymbol{G}$ is the flux corresponding to conservative variables $\boldsymbol{w}$ along the x direction. Then we can solve the Eq. (6) within the flux reconstruction framework, and the flux $\boldsymbol{G}$ can be computed using KIF.

B. Kinetic Iinviscid flux

The Riemann flux solver employed at the interfaces is one of the three critical factors of flux reconstruction method. In the present work, we implement the kinetic inviscid flux to determine the common flux at the interface of elements. The motivation of our work is to reach a compromise between good performance of the gas-kinetic scheme and lower computational costs. The KIF is a kind combination of the TTT scheme and the KFVS method.

The TTT scheme has been discussed by Xu in Ref. [50]. The first step of the TTT scheme is to get the Maxwellian distribution on both sides of the surface,

$$g_l = \left\{\rho\left(\frac{\lambda}{\pi}\right)^{\frac{K+1}{2}} e^{-[(u-U)^2+\xi^2]}\right\}_l,$$

$$g_r = \left\{\rho\left(\frac{\lambda}{\pi}\right)^{\frac{K+1}{2}} e^{-[(u-U)^2+\xi^2]}\right\}_r. \tag{7}$$

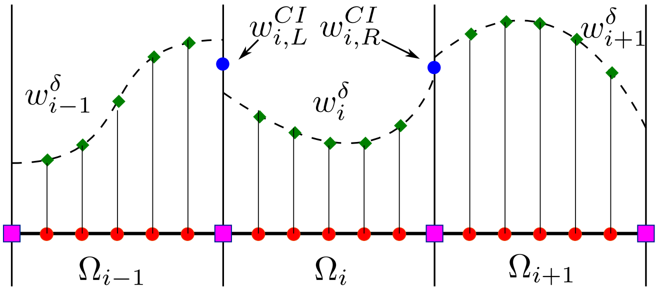

FIG. 1. The discontinuous solution polynomials and interface common solutions within elements Ω_{i-1}, Ω_i, and Ω_{i+1}.

The subscripts l and r represent the state based on the macroscopic variables from the left and right sides of the interface, respectively. The second step is to make particles cross the interface collide sufficiently. The new Maxwellian distribution g_0 is assumed to have the following form:

$$g_0 = \left\{\rho\left(\frac{\lambda}{\pi}\right)^{\frac{K+1}{2}} e^{-[(u-U)^2+\xi^2]}\right\}_0,$$

$$\boldsymbol{w}_0 = \int g_0\psi\, d\Xi = \int [(1-H(x)]g_l + H(x)g_r)\psi\, d\Xi, \qquad (8)$$

where $H(x)$ is the Heaviside function,

$$H(x) = \begin{cases} 0, & x < 0, \\ 1, & x \geqslant 0. \end{cases} \qquad (9)$$

Finally, the flux of the TTT scheme reads as

$$F_{\mathrm{TTT}} = \int u g_0 \psi\, d\Xi. \qquad (10)$$

The TTT scheme has a property similar to the central scheme, which does not introduce extra artificial viscosity in smooth flow area and can capture the boundary layer accurately. However, it cannot deal with shock wave, because it lacks artificial viscosity.

The equilibrium flux method (EFM) [51] and KFVS [52] are similar, and we just call it KFVS here. KFVS is another kinetic scheme and is a shock capturing method. After getting the Maxwellian distribution beside the interface using Eq. (7), KFVS gives flux by calculating particles across the interface as

$$F_{\mathrm{KFVS}} = \int_{u>0} u g_l \psi\, d\Xi + \int_{u<0} u g_r \psi\, d\Xi. \qquad (11)$$

KFVS has the properties of good robustness and positivity preservation [53], which make the scheme suitable for capturing the discontinuity. However, it introduces enormous artificial viscosity, and the essential problem, which is analyzed in Ref. [50], is that the equation solved at interface is the collisionless Boltzmann equation.

Combination is a good idea, which means that we use TTT in the smooth flow area and KFVS in the flow field where shock wave exists. The idea of KIF can be viewed as an inviscid-viscous splitting version of the gas-kinetic scheme, and Shu [54] and Ohwada [55] have made the fundamental contribution. The most significant difference between KIF [28] and the works of Shu and Ohwada is the weight of TTT and KFVS. Reference [28] adopted the philosophy of direct modeling [56] and constructed two kinds of KIF method (namely the KIF1 method from the GKS strategy [1] and the KIF2 method from the DUGKS strategy [57]). In the present work, we adopt the KIF1 method in the simulations. The KIF1 method can be expressed as

$$\boldsymbol{F} = \left\{\frac{\tau}{\delta t}(1 - e^{-\delta t/\tau})\right\}\boldsymbol{F}_{\mathrm{KFVS}} + \left\{1 - \frac{\tau}{\delta t}(1 - e^{-\delta t/\tau})\right\}\boldsymbol{F}_{\mathrm{TTT}}, \qquad (12)$$

$$\delta t = r\tau = \frac{\tau}{\max\limits_{\Omega}\left[\frac{|p_l - p_r|}{|p_l + p_r|}, \max(\mathrm{Ma}_l, \mathrm{Ma}_r)\right]}, \qquad (13)$$

where δt is the observation timescale and is measured in mean collision time (or the relaxation time τ) in discontinuities. For details of the KIF1 method, see Ref. [28].

In other words, KIF is a kind of balance between the kinetic scheme and the traditional macroscopic numerical method. In recent years, kinetic schemes have made a significant development [57–61] that mainly aims at nonequilibrium flow. With a view at equilibrium state, KIF replaces the complicated nonequilibrium part with the traditional central viscosity scheme. One motivation is to find a balance between advantages and efficiency, while another is to be suitable and easy to integrate into the existing framework.

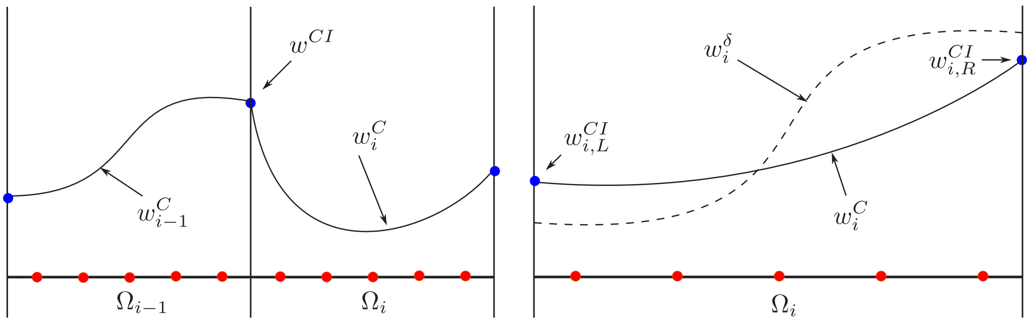

(a) (b)

FIG. 2. The demonstration of solution correction: (a) Corrected solution beside the interface and (b) the solution correction within element Ω_i.

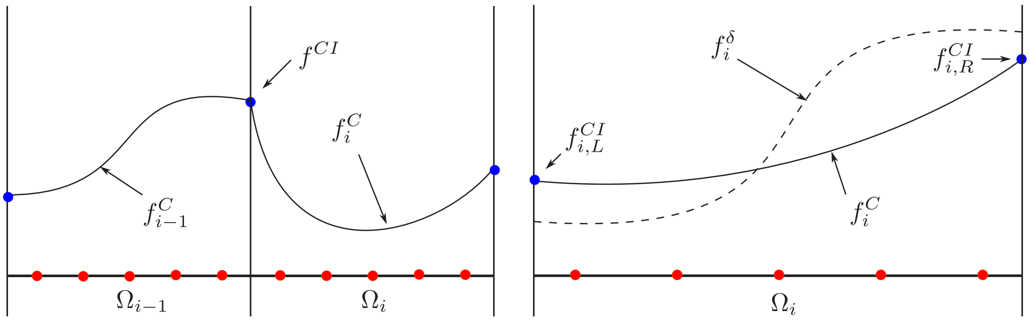

(a) (b)

FIG. 3. The demonstration of flux correction: (a) Corrected flux beside the interface and (b) the flux correction within element Ω_i.

C. Spatial discretization in flux reconstruction framework

In this section, the FR framework used to solve Eq. (6) is introduced. For the one-dimensional problem, the computational domain Ω can be divided into N subdomains,

$$\Omega = \{\Omega_i | i = 0, 1, \dots, N-1\},$$
$$\Omega_i = [x_i, x_{i+1}], \quad x_0 < x_1 < \cdots < x_N. \tag{14}$$

Within the element Ω_i, the solution points are set as $x_{i,k}$ ($k = 0, 1, 2, \dots, P$). It is obvious that the number of solution points within a standard elements is $P+1$, and P is related with the accuracy order of the numerical method. The set $x_{i,k}$ can be chosen as Gauss, Radau, Lobatto, or equidistant points. It has been proved in Refs. [43,44] by H. T. Huynh that Fourier stability and accuracy analysis of the FR framework are independent of the type of solution points.

Since dealing with every elements Ω_i is very tedious, all the element Ω_i should be mapped into the same standard element $\Omega_s = \{\xi | \xi \in [-1, 1]\}$ to simplify the implementation of the algorithm. The mapping function $\theta(\xi)$ can be expressed as

$$x = \theta_i(\xi) = \left(\frac{1-\xi}{2}\right)x_i + \left(\frac{1+\xi}{2}\right)x_{i+1}. \tag{15}$$

In order to be consistent with the existing literature of the FR framework, the denotation of flux $\boldsymbol{G}$ in Eq. (6) is replaced by $\boldsymbol{f}$. In present work, we apply KIF to compute the total flux $\boldsymbol{f}$. For the inviscid problem, $\boldsymbol{f}$ is computed using Eq. (12). For the viscous problem, the total flux $\boldsymbol{f}$ can be expressed as

$$\boldsymbol{f} = \boldsymbol{f}_c + \boldsymbol{f}_v, \tag{16}$$

where $\boldsymbol{f}_c$ is computed using Eq. (12), and the viscous part $\boldsymbol{f}_v$ has the following form:

$$\boldsymbol{f}_v = \boldsymbol{f}_{v,1} + \boldsymbol{f}_{v,2} + \boldsymbol{f}_{v,3}, \tag{17}$$

where

$$\boldsymbol{f}_{v,1} = \begin{pmatrix} 0, \\ \sigma_{xx} \\ \sigma_{xy} \\ \sigma_{xz} \\ U_i\sigma_{ix} - q_x \end{pmatrix}, \quad \boldsymbol{f}_{v,2} = \begin{pmatrix} 0, \\ \sigma_{yx} \\ \sigma_{yy} \\ \sigma_{yz} \\ U_i\sigma_{iy} - q_y \end{pmatrix},$$
$$\boldsymbol{f}_{v,3} = \begin{pmatrix} 0, \\ \sigma_{zx} \\ \sigma_{zy} \\ \sigma_{zz} \\ U_i\sigma_{iz} - q_z \end{pmatrix}. \tag{18}$$

The viscous stress reads

$$\sigma_{ij} = \mu\left(\frac{\partial U_i}{\partial x_j} + \frac{\partial U_j}{\partial x_i}\right) - \frac{2}{3}\mu\delta_{ij}\frac{\partial U_k}{\partial x_k}, \tag{19}$$

where δ_{ij} is the Kronecker symbol, U is the macroscopic velocity, and the heat fluxes are defined as

$$q_i = -k\frac{\partial T}{\partial x_i}, \tag{20}$$

where

$$k = \frac{C_p\mu}{\mathrm{Pr}}, \quad T = \frac{p}{\rho R}. \tag{21}$$

TABLE I. L_2 normal of density for the advection of density problem.

N	L_2	Order
10	2.711254×10^{-5}	–
20	1.004359×10^{-6}	4.754614
40	5.789748×10^{-8}	4.116630
80	3.339470×10^{-9}	4.115809
160	2.089252×10^{-10}	3.998561
320	1.310146×10^{-11}	3.995187
640	8.208407×10^{-13}	3.996481

TABLE II. $L2$ normal of density for the isentropic vortex problem.

N	L_2	Order
10	4.342904×10^{-3}	–
20	2.410620×10^{-4}	4.171184
40	1.488880×10^{-5}	4.017105
80	9.680808×10^{-7}	3.942956
160	7.091912×10^{-8}	3.770881

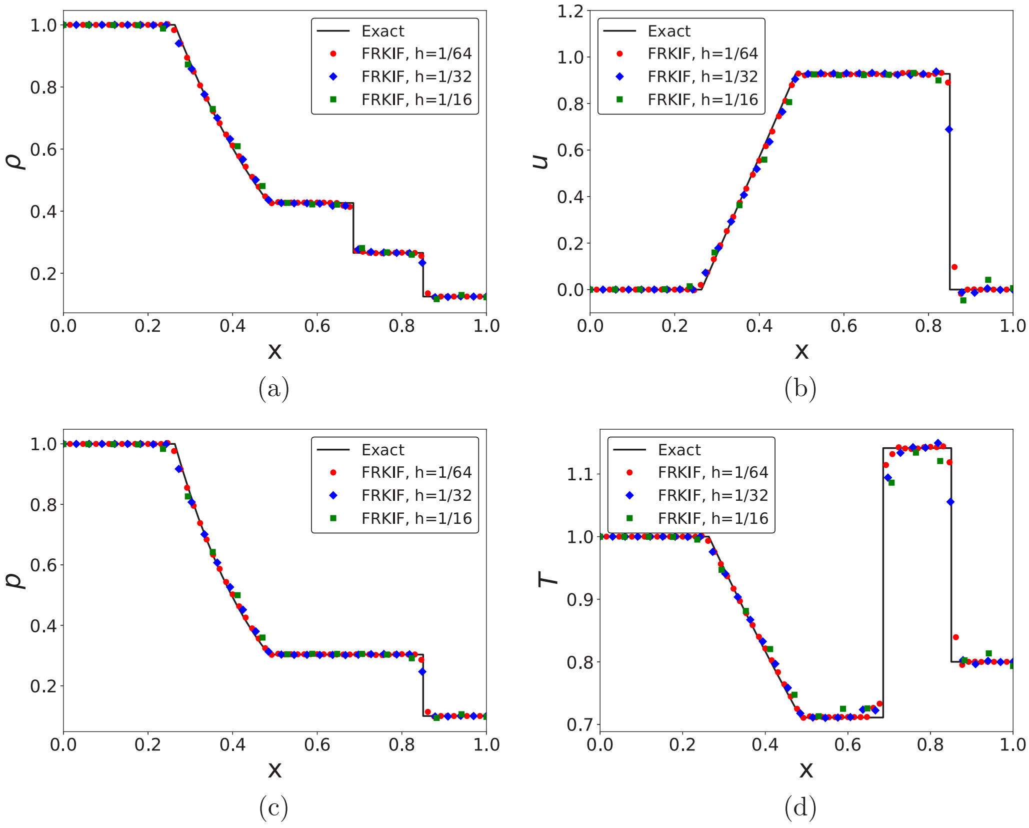

FIG. 4. The h criterion grid refinement tests for Sod shock tube problem: (a) density, (b) u-velocity, (c) pressure, and (d) temperature distributions at $t = 0.2$.

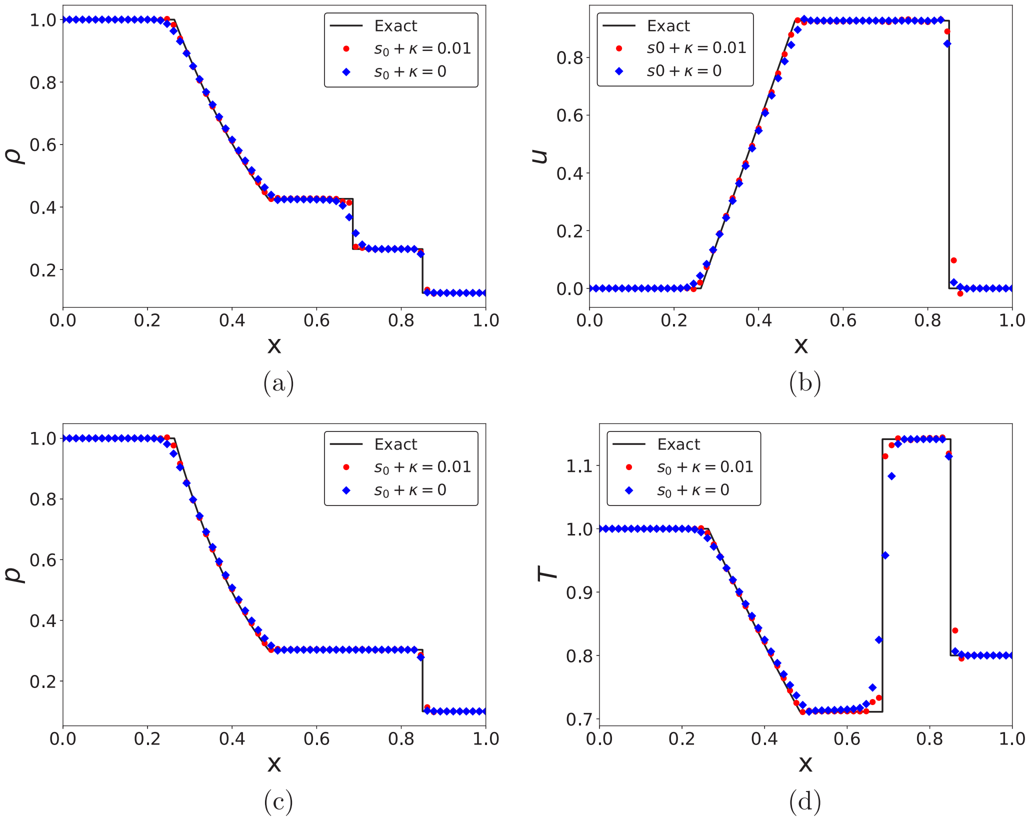

FIG. 5. The results of Sod shock tube problem with different values of $s_0 + \kappa$: (a) density, (b) u-velocity, (c) pressure, and (d) temperature distributions at $t = 0.2$. The length scale h is set as $1/64$.

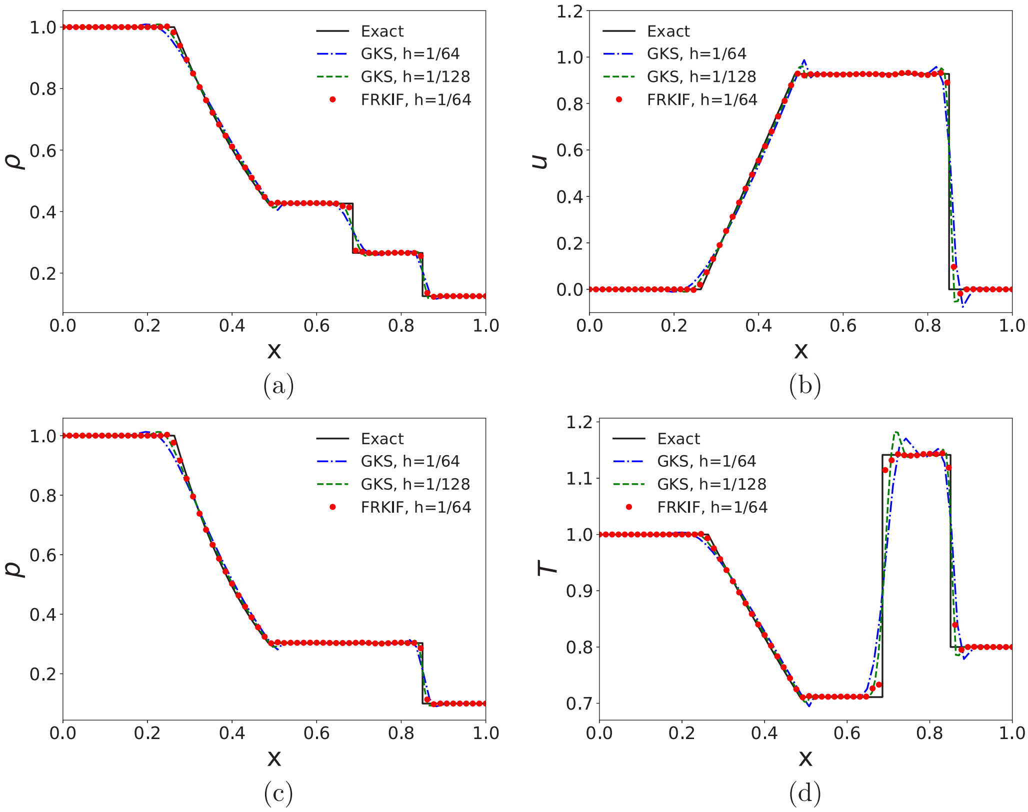

FIG. 6. The comparison between FRKIF and second-order gas-kinetic scheme: (a) density, (b) u-velocity, (c) pressure, and (d) temperature distributions at $t = 0.2$.

Pr represents the Prandtl number, C_p denotes the specific heat at constant pressure, and R is the gas constant.

With the mapping expressed as Eq. (15), the evolution of macroscopic variables $\boldsymbol{w}$ within each Ω_i can be transformed as the Eq. (22) within the standard element,

$$\hat{\boldsymbol{w}}_t + \frac{1}{J_n}\hat{\boldsymbol{f}}_\xi = 0, \tag{22}$$

where

$$\hat{\boldsymbol{w}} = \boldsymbol{w}(\theta_i(\xi), t) \quad \text{in} \quad \Omega_i, \tag{23}$$

$$\hat{\boldsymbol{f}} = \boldsymbol{f}(\theta_i(\xi), t) \quad \text{in} \quad \Omega_i, \tag{24}$$

$$J_n = \frac{\partial x}{\partial \xi} \quad \text{in} \quad \Omega_i. \tag{25}$$

The FR framework for solving the Eq. (22) within the standard element Ω_s consists of seven subsequent steps. In the first step, the solution polynomial $\hat{\boldsymbol{w}}_i^\delta(\xi)$ can be obtained through the macroscopic variable $\hat{\boldsymbol{w}}_{i,k}$ at the solution points ξ_k,

$$\hat{\boldsymbol{w}}_i^\delta(\xi) = \sum_{k=0}^{P} \hat{\boldsymbol{w}}_{i,k}\phi_k(\xi), \tag{26}$$

where the symbol δ denotes the solution polynomial, which is always discontinuous at the element interface. $\phi_k(\xi)$ is the 1D Lagrange polynomial equal to 1 at the kth solution point and 0 at the others,

$$\phi_k(\xi) = \prod_{l=0,l\neq k}^{P} \frac{\xi - \xi_l}{\xi_k - \xi_l}. \tag{27}$$

Figure 1 shows the solution polynomials at element Ω_i and the neighbors in the physical space. Take the interface $x_{i+1/2}$ as an example; $\boldsymbol{w}_i^\delta(x_{x+1/2})$ and $\boldsymbol{w}_{i+1}^\delta(x_{x+1/2})$ represent the macroscopic variables at the interface from Ω_i (left) and Ω_{i+1} (right), respectively. Generally speaking, $\boldsymbol{w}_i^\delta(x_{x+1/2})$ and $\boldsymbol{w}_{i+1}^\delta(x_{x+1/2})$ are not equal. Since ξ belongs to the

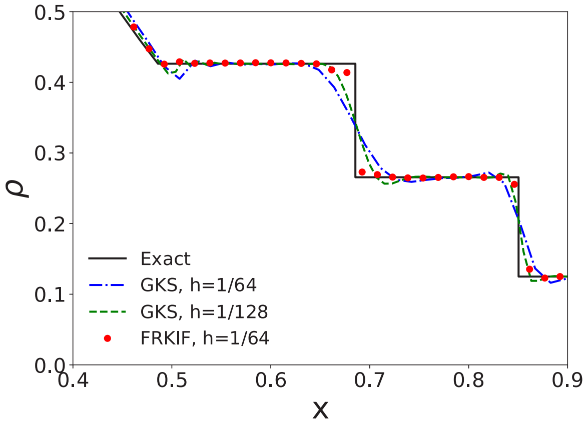

FIG. 7. The zoom in view of density distribution shown in Fig. 6(a).

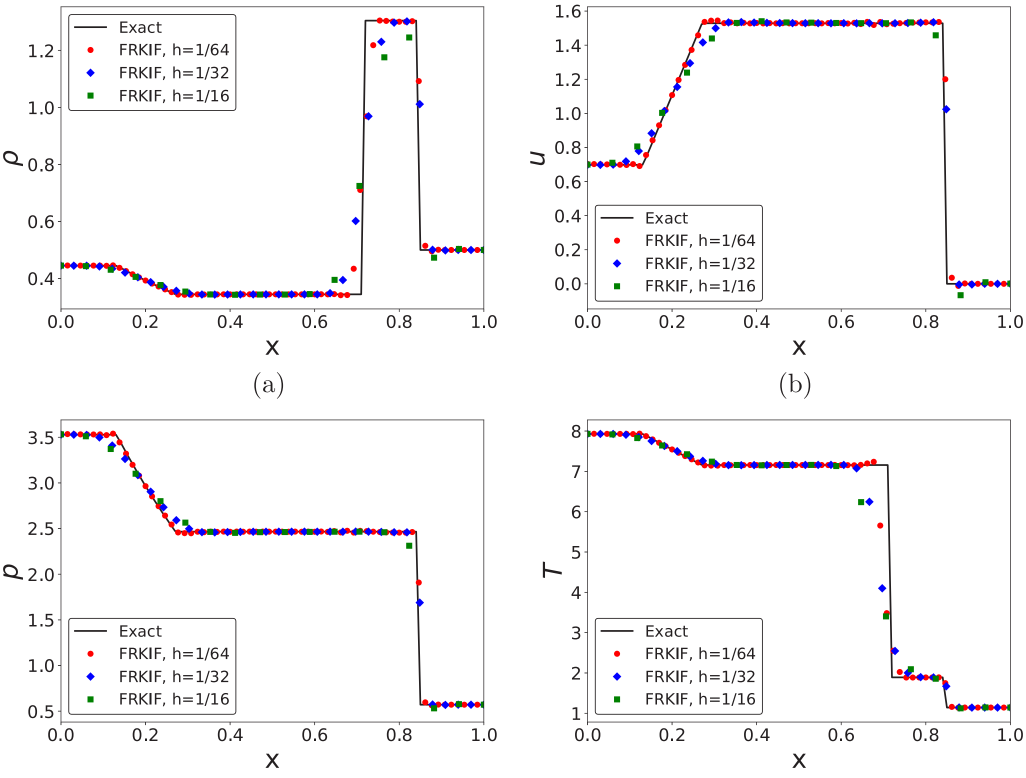

(a) (b)

(c) (d)

FIG. 8. The h criterion grid refinement tests for Lax problem: (a) density, (b) u-velocity, (c) pressure, and (d) temperature distributions at $t = 0.14$.

interval $[-1, 1]$ in the standard element Ω_s, $\boldsymbol{w}_i^\delta(x_{x+1/2})$ and $\boldsymbol{w}_{i+1}^\delta(x_{x+1/2})$ equal $\hat{\boldsymbol{w}}^\delta{}_i(1)$ and $\hat{\boldsymbol{w}}^\delta{}_{i+1}(-1)$ respectively. It is natural that $\hat{\boldsymbol{w}}^\delta{}_i(1)$ does not equal $\hat{\boldsymbol{w}}_{i+1}^\delta(-1)$ in most of cases, which is the "Discontinuous" at the interfaces of element.

In the second step, we must determine the common solution $\hat{\boldsymbol{w}}^{CI}$ at the boundaries of standard element, i.e., $\xi = \pm 1$. The common solution $\hat{\boldsymbol{w}}^{CI}$ at the interface is used to make the solution within the standard element to feel the effect of the boundaries, so the superscript C also has the meanings "corrected" and "continuous." In the present scheme, the common solution $\hat{\boldsymbol{w}}^{CI}$ is computed using the following expression:

$$\hat{\boldsymbol{w}}_{i+1/2}^{CI} = \int_{u>0} g_l \boldsymbol{\psi} d\,\Xi + \int_{u<0} g_r \boldsymbol{\psi} d\,\Xi, \tag{28}$$

where g_l and g_r, which correspond to $\hat{\boldsymbol{w}}_i(1)$ and $\hat{\boldsymbol{w}}_{i+1}(-1)$, are the Maxwellian distributions at the left and right sides of

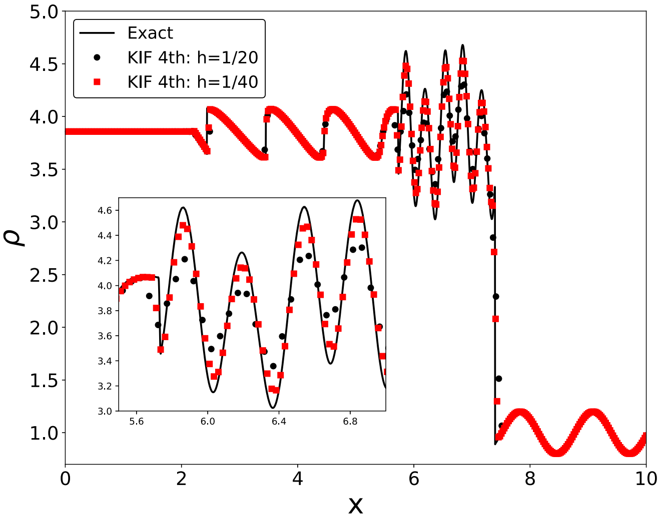

FIG. 9. Shu-Osher problem: The distribution of density-wave at $t = 1.8$.

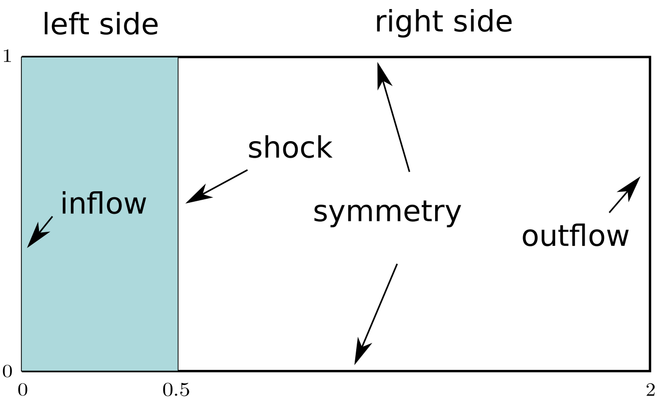

FIG. 10. Shock vortex interaction problem: The computational domain and the boundary conditions. In the simulation, Cartesian grid is used, and the element length scale of mesh h equals 1/100.

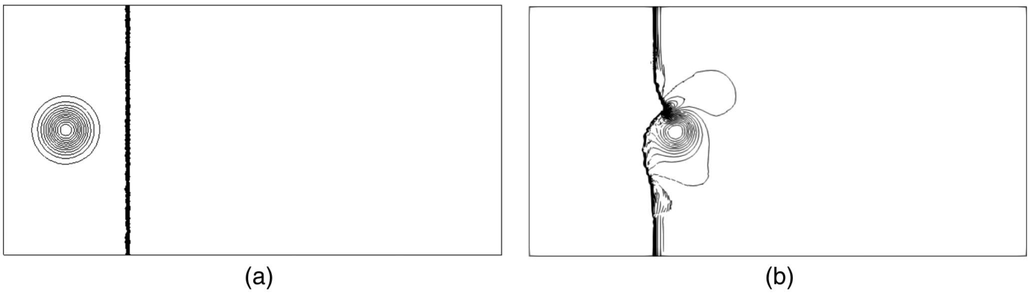
(a) (b)

FIG. 11. Shock vortex interaction problem: (a) The initial status and (b) the contour of pressure at $t = 0.3$.

an interface. $\hat{\boldsymbol{w}}_i^{\delta}(1)$ and $\hat{\boldsymbol{w}}_{i+1}^{\delta}(-1)$ can be obtained easily using Eq. (26). The demonstration of $\hat{\boldsymbol{w}}^{CI}$ is shown in Fig. 1.

It must be noted that if the jumps at boundaries of element are ignored, then the solution within the element cannot feel the effect of the boundaries and the evolution of scheme must get an erroneous result. Thus, the third step is to construct the corrected (or continuous) solution polynomial in the standard element. As shown in Fig. 1, the common solutions at the two end points of the element of Ω_i are $\hat{\boldsymbol{w}}_{i,L}^{CI}$ and $\hat{\boldsymbol{w}}_{i,R}^{CI}$, respectively. The corrected solution polynomial within the element is named $\hat{\boldsymbol{w}}_i^{C}(\xi)$ and has the following features:

$$\hat{\boldsymbol{w}}_i^{C}(-1) = \hat{\boldsymbol{w}}_{i-1/2}^{CI} = \hat{\boldsymbol{w}}_{i,L}^{CI}, \quad \hat{\boldsymbol{w}}_i^{C}(1) = \hat{\boldsymbol{w}}_{i+1/2}^{CI} = \hat{\boldsymbol{w}}_{i,R}^{CI}. \tag{29}$$

The corrected solution polynomial $\hat{\boldsymbol{w}}_i^{C}(\xi)$ is assumed to have the following form:

$$\hat{\boldsymbol{w}}_i^{C}(\xi) = \sum_{k=0}^{P} \hat{\boldsymbol{w}}_{i,k}\phi_k(\xi) + \left[\hat{\boldsymbol{w}}_i^{C}(-1) - \hat{\boldsymbol{w}}_i^{\delta}(-1)\right]\mathcal{G}_L(\xi) + \left[\hat{\boldsymbol{w}}_i^{C}(1) - \hat{\boldsymbol{w}}_i^{\delta}(1)\right]\mathcal{G}_R(\xi). \tag{30}$$

$\mathcal{G}_L(\xi)$ and $\mathcal{G}_R(\xi)$ are the correct functions related with the left and the right end points of the element, and $\mathcal{G}_L(\xi)$ and $\mathcal{G}_R(\xi)$ should satisfy the following conditions:

$$\mathcal{G}_L(-1) = 1, \quad \mathcal{G}_L(1) = 0, \quad \mathcal{G}_R(-1) = 0, \quad \mathcal{G}_R(1) = 1. \tag{31}$$

The correct function is one of the critical factors of the FR framework. For more details and introductions of correct function, see Refs. [43,44]. Now that the corrected solution polynomial is computed, the corrected solution derivatives polynomial $\frac{d\hat{\boldsymbol{w}}_i^{C}(\xi)}{d\xi}$ can be obtained directly,

$$\frac{d\hat{\boldsymbol{w}}_i^{C}(\xi)}{d\xi} = \sum_{k=0}^{P} \hat{\boldsymbol{w}}_{i,k}\frac{d\phi_k(\xi)}{d\xi} + \left[\hat{\boldsymbol{w}}_i^{C}(-1) - \hat{\boldsymbol{w}}_i^{\delta}(-1)\right]\frac{d\mathcal{G}_L(\xi)}{d\xi} + \left[\hat{\boldsymbol{w}}_i^{C}(1) - \hat{\boldsymbol{w}}_i^{\delta}(1)\right]\frac{d\mathcal{G}_R(\xi)}{d\xi}. \tag{32}$$

The correction procedure can be seen in Fig. 2 briefly.

The fourth step is to compute the flux $\hat{\boldsymbol{f}}_{i,k}$ at the solution point ξ_k. $\hat{\boldsymbol{f}}_{i,k}$ can be evaluated by the macroscopic variables $\boldsymbol{w}_{\hat{i},k}$ and the corrected derivatives $\frac{d\hat{\boldsymbol{w}}_i^{C}}{d\xi}(\xi_k)$, and $\frac{d\hat{\boldsymbol{w}}_i^{C}}{d\xi}(\xi_k)$ is computed from Eq. (32). To compute $\hat{\boldsymbol{f}}_{i,k}$, a KIF flux solver is used. After the fluxes at solution points have been computed, the flux polynomial within the element can be obtained,

$$\hat{\boldsymbol{f}}_i^{\delta}(\xi) = \sum_{k=0}^{P} \hat{\boldsymbol{f}}_{i,k}\phi_k(\xi). \tag{33}$$

$\hat{\boldsymbol{f}}_i^{\delta}$ means that the flux polynomial is always discontinuous at the boundaries of elements.

The fifth step focuses on the common flux $\hat{\boldsymbol{f}}^{CI}$ at the two end points of the element. The fluxes across the boundaries of elements are always discontinuous. To make the fluxes within an element feel the effect of the boundaries, it is very important to compute the continuous (or common) fluxes at the interface to get the accurate results. The common fluxes at boundaries of elements is another critical factor of the FR framework. Take the flux $\hat{\boldsymbol{f}}_{i+1/2}^{CI}$ as an example; $\hat{\boldsymbol{f}}_i^{\delta}(1)$, $\hat{\boldsymbol{f}}_{i+1}^{\delta}(-1)$, and $\hat{\boldsymbol{w}}_{i+1/2}^{CI}$ are needed. $\hat{\boldsymbol{f}}_i^{\delta}(1)$ and $\hat{\boldsymbol{f}}_{i+1}^{\delta}(-1)$ are evaluated using Eq. (33). In our present work, the KIF method is applied to compute $\hat{\boldsymbol{f}}_{i+1/2}^{CI}$.

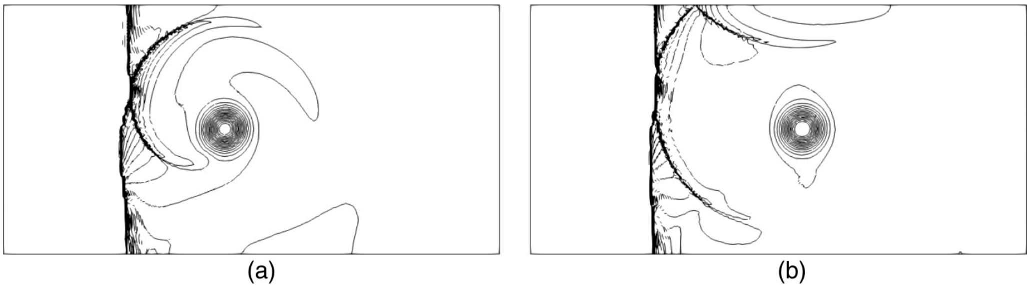
(a) (b)

FIG. 12. Shock vortex interaction problem: (a) The contours of pressure at $t = 0.6$ and (b) the contours of pressure at $t = 0.8$.

The sixth step is to correct the fluxes using the common fluxes at the interfaces. The procedure of flux correction is very similar to solution correction, and Fig. 3 exhibits the procedure primitively. The corrected flux polynomial reads

$$\hat{\boldsymbol{f}}_i^C(\xi)=\sum_{k=0}^{P}\hat{\boldsymbol{f}}_{i,k}\phi_k(\xi)+\left[\hat{\boldsymbol{f}}_i^C(-1)-\hat{\boldsymbol{f}}_i^\delta(-1)\right]\mathcal{H}_L(\xi)+\left[\hat{\boldsymbol{f}}_i^C(1)-\hat{\boldsymbol{f}}_i^\delta(1)\right]\mathcal{H}_R(\xi),\tag{34}$$

where $\mathcal{H}$ is the correction function, which is similar to the $\mathcal{G}$ used in the correction procedure of solution polynomial and $\mathcal{H}_L(\xi)$ and $\mathcal{H}_R(\xi)$ should satisfy the following conditions:

$$\mathcal{H}_L(-1)=1,\quad \mathcal{H}_L(1)=0,\quad \mathcal{H}_R(-1)=0,\quad \mathcal{H}_R(1)=1.\tag{35}$$

The final step is to compute the divergence of the corrected fluxes at the solution points. Since the corrected flux polynomial is expressed as Eq. (34), the divergence of the corrected flux at the solution point ξ_k can be obtained directly,

$$\hat{\boldsymbol{f}}_{\xi,i,k}=\frac{d\hat{\boldsymbol{f}}_i^C}{d\xi}(\xi_k)=\sum_{k=0}^{P}\hat{\boldsymbol{f}}_{i,k}\frac{d\phi_k}{d\xi}(\xi_k)+\left[\hat{\boldsymbol{f}}_i^C(-1)-\hat{\boldsymbol{f}}_i^\delta(-1)\right]\frac{d\mathcal{H}_L}{d\xi}(\xi_k)+\left[\hat{\boldsymbol{f}}_i^C(1)-\hat{\boldsymbol{f}}_i^\delta(1)\right]\frac{d\mathcal{H}_R}{d\xi}(\xi_k).\tag{36}$$

By now, all the preconditions of using Eq. (22) to update the macroscopic variables at the solution points are completed for the 1D advection problem.

D. VCJH scheme

The correction function is critical for the flux reconstruction method. $\mathcal{G}$ and $\mathcal{H}$ have a great effect on the accuracy and stability. The VCJH scheme developed by Vincent [45] is used in our work. The correction function of VCJH scheme is defined as

$$\mathcal{G}_L=\frac{(-1)^P}{2}\left[\Psi_P-\left(\frac{\eta_P\Psi_{P-1}+\Psi_{P+1}}{1+\eta_P}\right)\right],\tag{37}$$

and

$$\mathcal{G}_R=\frac{1}{2}\left[\Psi_P+\left(\frac{\eta_P\Psi_{P-1}+\Psi_{P+1}}{1+\eta_P}\right)\right],\tag{38}$$

where

$$\eta_P=\frac{\varepsilon(2P+1)(a_PP!)^2}{2},\quad a_P=\frac{(2P)!}{2^P(P!)^2},\tag{39}$$

where P is the order of polynomial and Ψ_P is the P order Legendre polynomial. In order for the scheme to be stable, the parameter ε must be within the range $\varepsilon_{\_}<\varepsilon<\infty$, where

$$\varepsilon_{\_}=\frac{-2}{(2P+1)(a_PP!)^2}.\tag{40}$$

The VCJH scheme has been proved as an energy stable scheme, and it can be recovered to a particular existing scheme, such as nodal DG ($\varepsilon=0$). The correction function $\mathcal{H}$ is similar to $\mathcal{G}$.

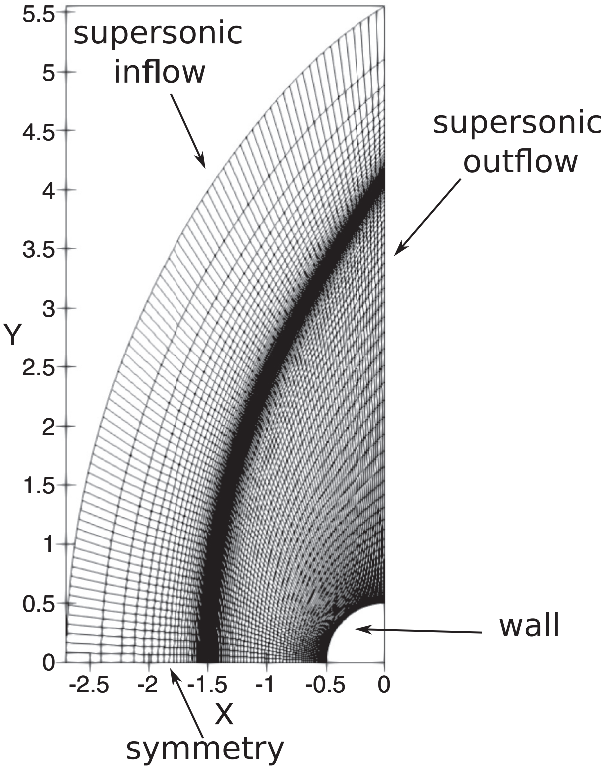

FIG. 13. The computational domain and boundary conditions used in the simulation of supersonic flow past a circular cylinder.

E. Time marching method

In terms of time integration, an explicit Runge-Kutta method [62] is used in the present work. Equation (22) can be rewritten as

$$\hat{\boldsymbol{w}}_t=-\frac{1}{J_n}\hat{\boldsymbol{f}}_\xi=\mathcal{L}(\hat{\boldsymbol{w}}).\tag{41}$$

The time marching method is expressed as

$$\begin{aligned}
\hat{\boldsymbol{w}}^{(1)}&=\hat{\boldsymbol{w}}^{(0)}+\frac{1}{2}\Delta t\mathcal{L}(\hat{\boldsymbol{w}}^{(0)}),\\
\hat{\boldsymbol{w}}^{(2)}&=\hat{\boldsymbol{w}}^{(0)}+\frac{1}{2}\Delta t\mathcal{L}(\hat{\boldsymbol{w}}^{(1)}),\\
\hat{\boldsymbol{w}}^{(3)}&=\hat{\boldsymbol{w}}^{(0)}+\Delta t\mathcal{L}(\hat{\boldsymbol{w}}^{(2)}),\\
\hat{\boldsymbol{w}}^{(4)}&=\frac{1}{3}\left[-\hat{\boldsymbol{w}}^{(0)}+\hat{\boldsymbol{w}}^{(1)}+2\hat{\boldsymbol{w}}^{(2)}+\hat{\boldsymbol{w}}^{(3)}\right]+\frac{1}{6}\Delta t\mathcal{L}(\hat{\boldsymbol{w}}^{(3)}),
\end{aligned}\tag{42}$$

where $\hat{\boldsymbol{w}}^{(0)}=\hat{\boldsymbol{w}}^n$ and $\hat{\boldsymbol{w}}^{(4)}=\hat{\boldsymbol{w}}^{n+1}$.

F. Extension to multidimensional problem

Extension to quadrilateral and hexahedral elements are straightforward [43,44]. Take the hexahedral elements as example; the interpolation polynomial of solution is obtained by tensor products of the one-dimensional interpolation basis,

$$\hat{\boldsymbol{w}}^\delta(\xi,\eta,\zeta)=\sum_{i=0}^{P}\sum_{j=0}^{P}\sum_{k=0}^{P}\hat{\boldsymbol{w}}_{i,j,k}\phi_i(\xi)\phi_j(\eta)\phi_k(\zeta),\tag{43}$$

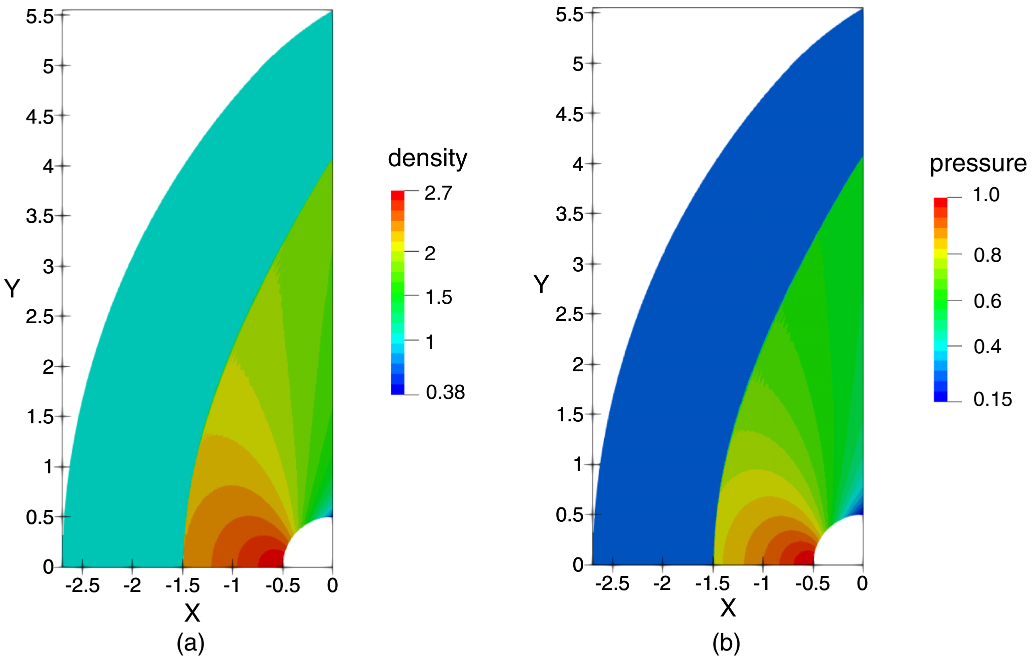

(a) (b)

FIG. 14. Numerical results of the supersonic flow over a circular cylinder: (a) density and (b) pressure.

where i, j, and k are the indexes along the three axis, respectively. The interpolation polynomial of flux is as same as solution polynomial.

For triangles [47,63] and tetrahedra [64], they are more complicated in algorithm and implementation. But the procedure is analogous to FR in one dimension.

The correction function for hexahedral elements is as similar as Eq. (43), which can be written as

$$\mathcal{G}(\xi,\eta,\zeta)=\sum_{i=0}^{P}\sum_{j=0}^{P}\sum_{k=0}^{P}\mathcal{G}_{i,j,k}\phi_i(\xi)\phi_j(\eta)\phi_k(\zeta). \tag{44}$$

For details on extension to multiple dimensions, see Ref. [43].

G. Shock capturing method

Robust shock capturing is a main difficulty for the high-order FE-type CFD method. In the vicinity of discontinuities, the smooth indicator [65–67] is used to detect the discontinuity. Once the shock has been sensed, the shock capturing method is applied on the elements. In the present work, we follow the idea of Sheshadri and Jameson [67]. We use two parameters s_0 and κ to decide whether the shock capturing method should be applied. For the determination of values s_0 and κ, see Refs. [68,69]. In the present paper, we set $s_0+\kappa$ around the value 0.01. We find that this setting can keep the scheme robust and accurate.

TABLE III. The details of the grids used in the laminar boundary layer case.

	Grid size	Number of elements in boundary layer
Grid 1	4876	25
Grid 2	2336	6

III. NUMERICAL TEST CASES

In this section, numerical tests are set up for the validation of present method. The accuracy order, shock capturing method, viscous flow problem, and various boundary conditions are all validated in the section. Finally, the potential of present scheme to simulate the turbulent flow is verified in the Taylor-Green vortex problem.

Our algorithmic code is deployed on the HiFiLES open-source platform [70]. It should also be noted that the polynomial order $p=3$ is used in this section. Several one-dimensional problems are simulated using multidimensional code in the present paper. The upper and bottom bounds of the computational domain are treated as periodic boundaries in these cases.

A. Accuracy tests

In this case, the advection of density perturbation problem [19] is presented to validate the accuracy of our method on Cartesian grid. The initial condition is given as

$$\rho(x)=1+0.2\sin(\pi x),\quad u(x)=1,\quad v(x)=0,\quad p(x)=1, \tag{45}$$

and the analytic solution at the time t can be expressed as

$$\rho(x,t)=1+0.2\sin(\pi(x-t)),\quad u(x,t)=1,\quad v(x,t)=0,\quad p(x,t)=1. \tag{46}$$

The case is a one-dimensional problem, and we simulate it using a two-dimensional solver on the Cartesian grid. The computational domain is

$$\{(x,y)|x\in[0,1],y\in[0,4h]\}, \tag{47}$$

where the length scale h equals $1/N$. N is the number of elements along the x direction. Table I gives the L_2 normal

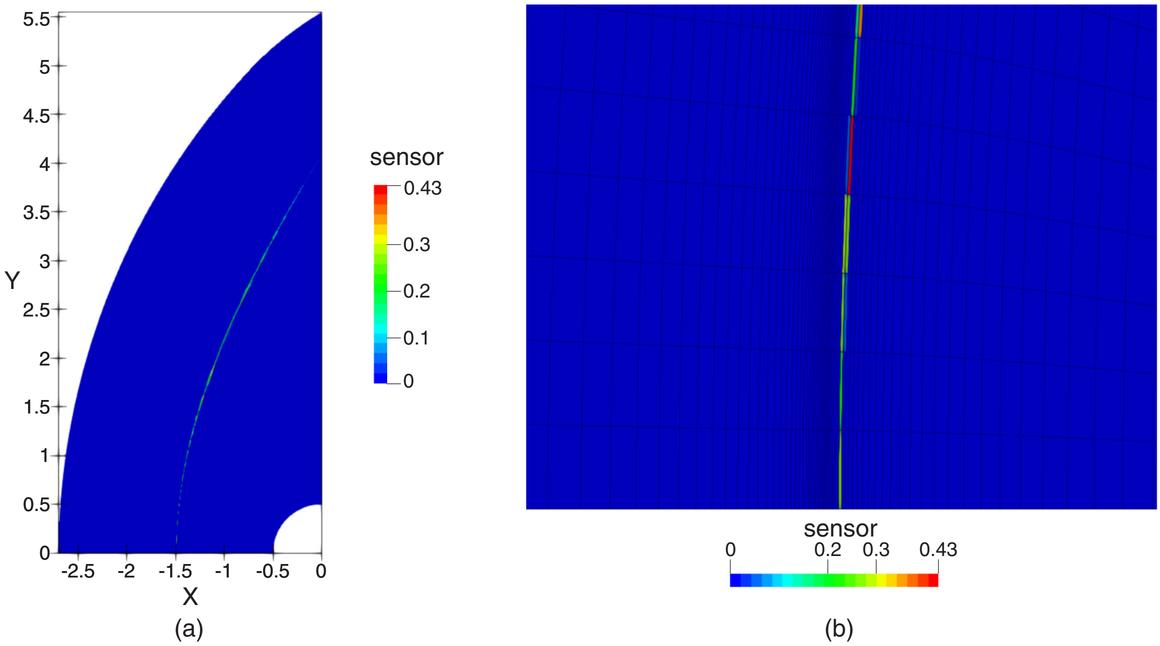

(a)

(b)

FIG. 15. The sensor values in the simulation of supersonic flow over a circular cylinder: (a) full domain and (b) zoom in view.

of density distribution. The numerical results are obtained at $t = 2$, and the time step is set as $\Delta t = 0.05/N$. It can be concluded from Table I that the accuracy order is reached quite well.

The second case is the isentropic vortex problem, which is a two-dimensional problem always used to validate the accuracy of high-order method. The computational domain is a $[-5, 5] \times [-5, 5]$ square. The periodic boundary is applied on the four bounds of the square. The diagonal uniform form flow, $(\rho, u, v, p) = (1, 1, 1, 1)$, is initialed in the flow field. Then a small perturbation is added to the center of the square,

$$(\delta u, \delta v) = \frac{\epsilon}{2\pi} e^{(0.5(1-r^2))}(-y, x), \tag{48}$$

$$\delta T = -\frac{(\gamma - 1)\epsilon^2}{8\gamma\pi^2} e^{(1-r^2)}, \qquad \delta S = 0. \tag{49}$$

where

$$r^2 = (x^2 + y^2).$$

Since the vortex is moved along the diagonal line with the time marching in the case, the numerical results is obtained at $t = 10$. The vortex is just back to the origin position at the moment. The triangular grid, which is similar to the grid shown in Fig. 17, is used in the simulation. The time step is set as $\Delta t = 0.01/N$. N is the number of elements on the bound. Table II gives the L_2 normal of density. The designed accuracy order can be clearly seen in the table.

B. One-dimensional Riemann problem

The first one-dimensional Riemann problem is the Sod shock tube problem [71], which is always used to validate the ability of numerical schemes to capture the discontinuity. The computational domain is $(x, y) \in [0, 1] \times [0, 4h]$, and the Cartesian grids with different length scale h are used in the approach. The initial condition reads

$$(\rho, u, v, p) = \begin{cases} (1, 0, 0, 1), & 0 < x < 0.5, \\ (0.125, 0, 0, 0.1), & 0.5 \leqslant x \leqslant 1. \end{cases} \tag{50}$$

Figure 4 shows the density, velocity, pressure, and temperature distributions at $t = 0.2$. The numerical results have a good accordance with the exact solution, and it can be obviously seen that the accuracy is improved with the h criterion grid refinement. For the shock capturing method used in the present work, the value of $s_0 + \kappa$ has a great effect on the numerical accuracy. It is well known that when we set $s_0 + \kappa$ to a larger value, we obtain greater accuracy. Figure 5 plots the simulation with different values of $s_0 + \kappa$. It is evident that the higher accuracy can be obtained with the larger value of $s_0 + \kappa$.

Figure 6 shows the comparison between present method and second-order gas-kinetic scheme. For the present method,

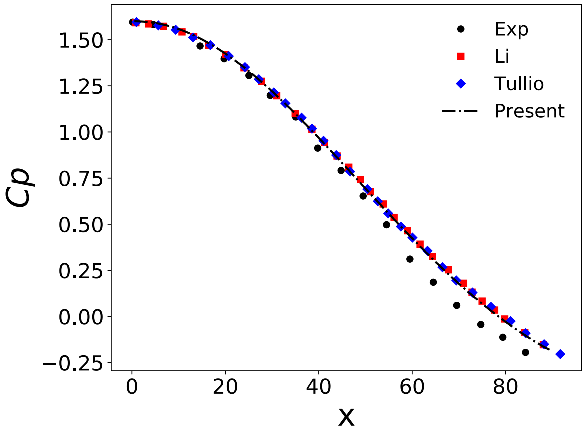

FIG. 16. The pressure coefficient on the surface of circular cylinder.

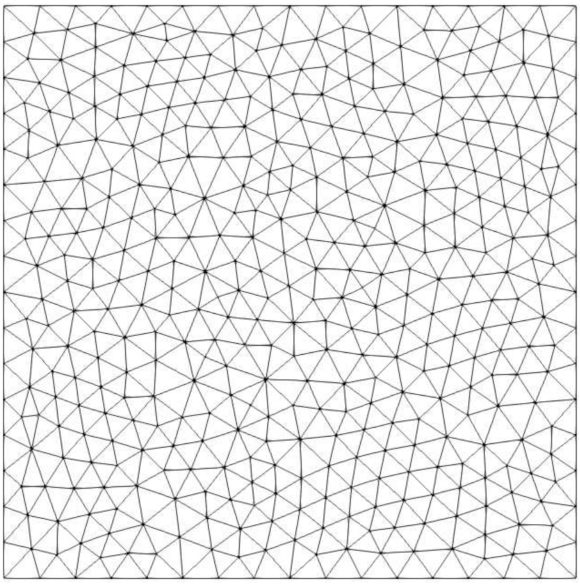

FIG. 17. The triangular grid used in the simulation of lid-driven cavity flow (816 triangular elements).

the numerical results is obtained using the grid with $h = 1/64$. Compared with the data computed using GKS with the same grid ($h = 1/64$) and refined grid ($h = 1/128$), the present method can approach the exact solution more accurately. The accuracy of present method has been confirmed. It also can be seen from the Fig. 6 that the oscillation near the discontinuity is suppressed very well. Figure 7 shows the zoom in view of density distribution. It is clear that the discontinuity can be captured very well within three points.

The second one-dimensional Riemann problem is the Lax problem [72]. Compared with Sod shock tube problem, the Lax problem has a much stronger discontinuity. The computational domain is $(x, y) \in [0, 1] \times [0, 4h]$, and the Cartesian grids with different length scale h are used in the approach. The value of $s_0 + \kappa$ is set as 0.01 in the computation.

The initial condition is expressed as

$$(\rho, u, v, p) = \begin{cases} (0.445, 0.698, 0.0, 3.528), & 0 < x < 0.5, \\ (0.5, 0.0, 0.0, 0.571), & 0.5 \leqslant x \leqslant 1. \end{cases} \tag{51}$$

Figure 8 shows the density, velocity, pressure, and temperature distributions at $t = 0.14$. The numerical results have a good accordance with the exact solution. The little oscillation can be seen nearby the discontinuity, and it is because that the shock is not captured very well. The shock capturing method is an open question needed to be further studied.

C. Shu-Osher problem

The problem of Shu-Osher [72] describes the interaction of a sinusoidal density wave with a Mach 3 normal shock. The purpose of this case is to validate the behavior of our method on the shock-wave interaction problem. The shock capturing method is also examined in the case, and $s_0 + \kappa$ is set as 0.01 in the simulation. The computational domain used in the simulation is taken as $[0, 10] \times [0, 4h]$. The Cartesian grid is used in the simulations, and the length scale of the grid is $h = 1/20, 1/40$. The upper and the bottom boundaries are set as the periodic boundary, and the left and right sides are set as the nonreflecting boundary. The initial condition is given as

$$(\rho, u, v, p) = \begin{cases} (3.857143, 2.629369, 0.0, 10.33333), & 0 \leqslant x < 1, \\ (1 + 0.2\sin(5(x - 4)), 0.0, 0.0, 1.0), & 1 \leqslant x \leqslant 10. \end{cases} \tag{52}$$

Figure 9 shows the density distribution at $t = 1.8$, and the zoom in view near the high-frequency wave is also exhibited. Because the exact solution of this problem cannot be computed directly, the solution of fourth-order WENO method with 10 000 grid points in one dimension is taken as the exact result. It can be seen in Fig. 9 that the performance is improved with increasing mesh resolution. The discontinuity is captured well, and the ability of present scheme to capture the frequency wave is also be verified in the case.

D. Shock vortex interaction problem

The shock vortex interaction problem [35] is always used to validate the performance of the high-order method. Compared to the lower-order method, the high-order scheme has the advantage of resolving the vortex and interaction.

In the simulation, a stationary normal shock and a small perturbation are initialed in the flow field. A Mach 1.1 normal shock wave is located at the position $x = 0.5$. The left-side state (Ma = 1.1) of the shock wave is given as follows:

$$(\rho, u, v, p) = (\mathrm{Ma}^2, \sqrt{\gamma}, 0.0, 1.0), \quad T = p/\rho,$$
$$S = \ln(p/\rho^\gamma). \tag{53}$$

A small and weak vortex is superposed to the left side of the normal shock. The center of the vortex is $(x_c, y_c) = (0.25, 0.5)$. The perturbation is given as

$$(\delta u, \delta v) = \kappa \eta e^{\mu(1-\eta^2)}(\sin\theta, -\cos\theta), \tag{54}$$

$$\delta T = -\frac{(\gamma - 1)\kappa^2}{4\mu\gamma} e^{2\mu(1-\eta^2)}(\sin\theta, -\cos\theta), \quad \delta S = 0, \tag{55}$$

where

$$\kappa = 0.3, \quad \mu = 0.204, \quad \eta = r/r_c,$$
$$r_c = 0.05, \quad r = \sqrt{(x - x_c)^2 + (y - y_c)^2}. \tag{56}$$

The computational domain and boundary conditions are exhibited in the Fig. 10. In the simulation, the Cartesian grid is used and the grid size h is 1/100. To capture the

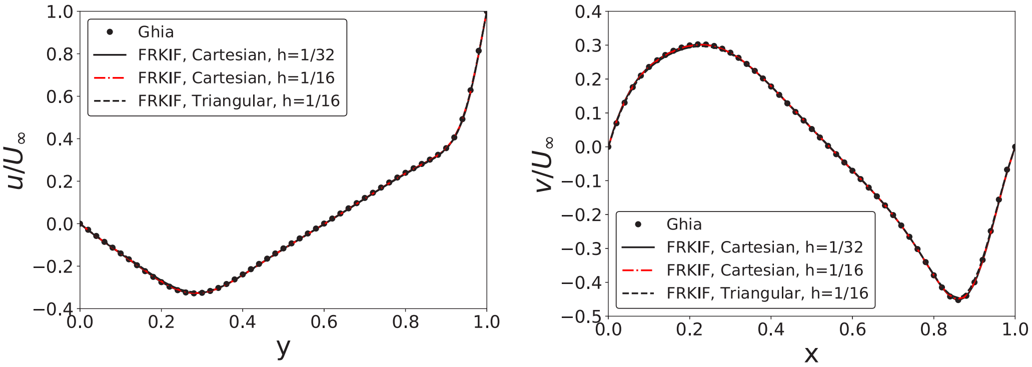

(a) (b)

FIG. 18. The velocity profile of the lid-driven cavity flow at Re = 400: (a) u-velocity profiles at $x = 0.5$ and (b) v-velocity profiles at $y = 0.5$.

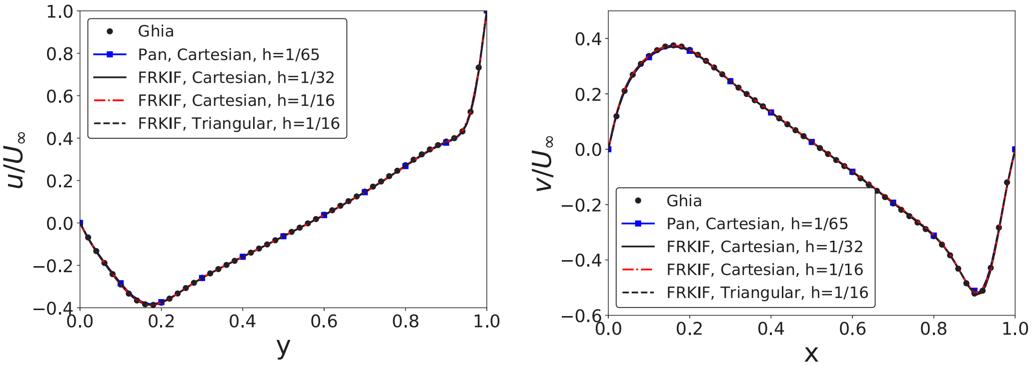

(a) (b)

FIG. 19. The velocity profile of the lid-driven cavity flow at Re = 1000: (a) u-velocity profiles at $x = 0.5$ and (b) v-velocity profiles at $y = 0.5$.

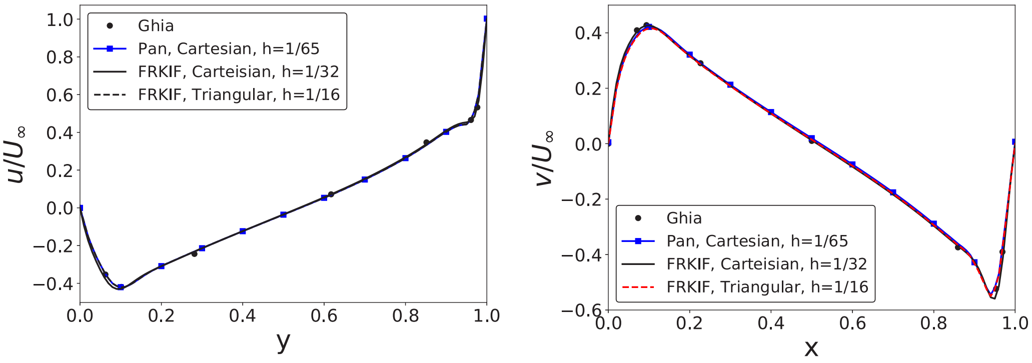

(a) (b)

FIG. 20. The velocity profile of the lid-driven cavity flow at Re = 3200: (a) u-velocity profiles at $x = 0.5$ and (b) v-velocity profiles at $y = 0.5$.

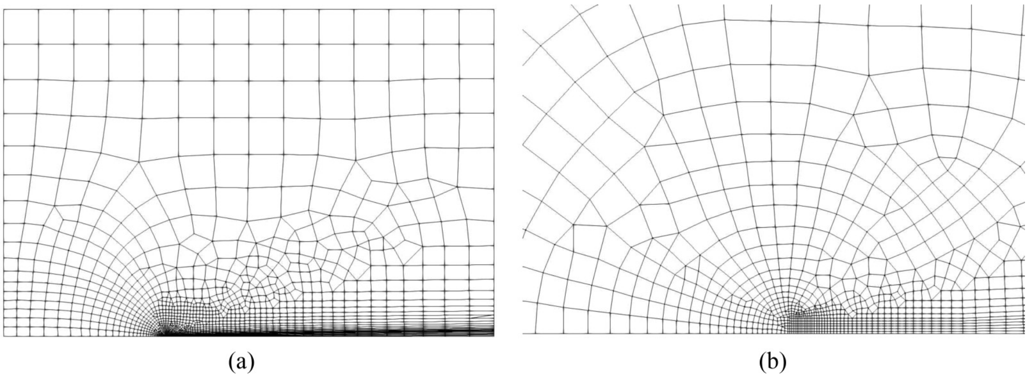
(a) (b)

FIG. 21. The "Grid 2" used in the simulation of laminar flow over a flat plate.

discontinuity, the coefficient $s_0 + \kappa$ is set as 0.01. The initial status at $t = 0$ and the contour plots at $t = 0.3$, $t = 0.6$, and $t = 0.8$ are shown in Fig. 11 and Fig. 12. The perturbation is initialed at $t = 0$, and then the vortex moves from left to right across the shock. The profile of vortex varies with the movement, and the interaction of shock and vortex can be seen obviously in the Fig. 11 and Fig. 12. The plots show that our present method can capture the shock and vortex interaction with enough resolution, and the vortex is recovered well. It also shows clearly in Fig. 12 that the shock bifurcations reaches to the top boundary, and the reflection is evident.

E. Supersonic flow past a circular cylinder

The supersonic flow past a circular cylinder is used to validated proposed method for the two-dimensional compressible flow with shock wave. In the simulation, the Mach number of free stream flow is 1.7, and the Reynolds number is 2.0×10^5. The diameter of the cylinder is $D = 1$. The computational domain and boundary conditions are shown in Fig. 13. The quadrilateral mesh is used in the simulation, and the shock wave region is refined to capture the bow shock wave. The cell number of the grid is 9638 and the minimum distance to the surface of cylinder is 0.0008.

The free stream flow encounters a bow shock wave ahead of the cylinder. The shock wave is located at $x/D \approx -1.5$ in front of the cylinder. In Fig. 14 the contours of density and pressure of the flow field are shown. The shock wave can be seen clearly in the figure, and the position of the shock wave is identical to the Ref. [73]. To capture the shock wave, the shock capturing technique is adopted. Figure 15 shows the shock sensor values of elements. It is evident that the shock sensor can distinguish between shock and smooth region. We can find from Fig. 15(b) that the shock spreads within three cells.

Figure 16 shows the pressure coefficient on the surface of the circular cylinder. The experimental data is extracted from Ref. [74]. It is obviously that the results of present method has a good agreement with the results of Tullio *et al.* [73] and Li [75]. For the lack of three-dimensional effect, all the numerical results are a little larger than the experimental data.

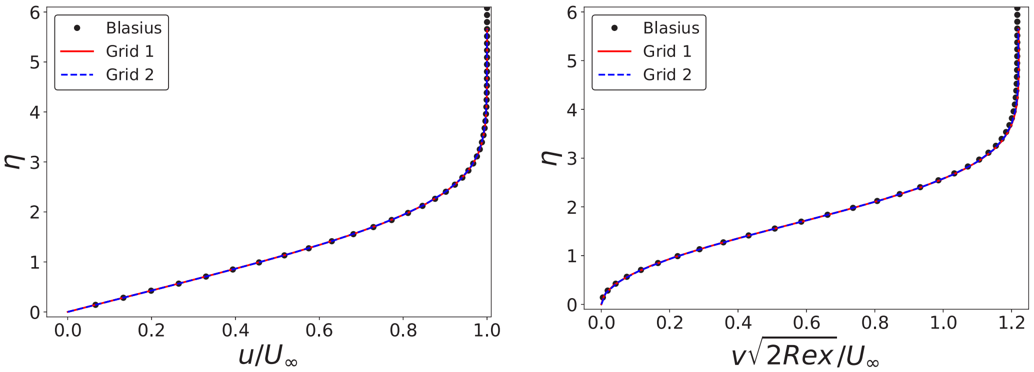

(a) (b)

FIG. 22. Blasius incompressible laminar flat plate: (a) u-velocity and (b) v-velocity profiles at $x/L = 0.1$.

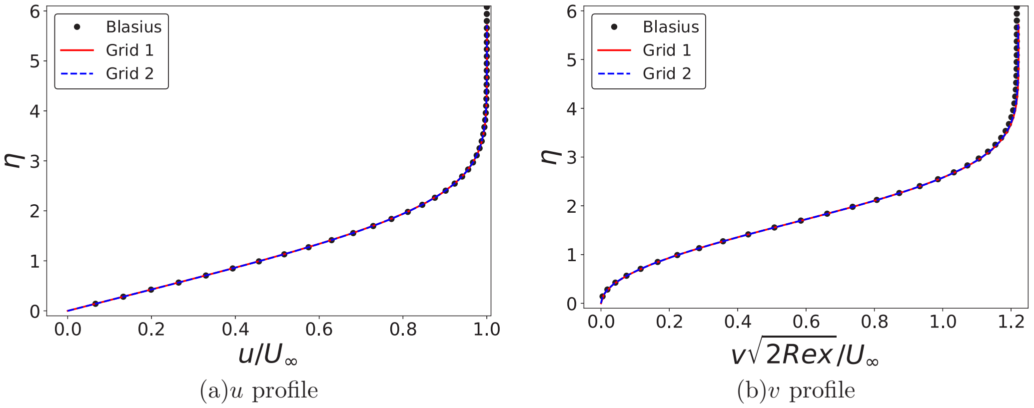

(a)u profile (b)v profile

FIG. 23. Blasius incompressible laminar flat plate: (a) u-velocity and (b) v-velocity profiles at $x/L = 0.3$.

F. Lid-driven cavity flow

The lid-driven cavity flow [76] is one of the benchmarks for validating the performance of the viscous flow solver, and the aim of this case is also to examine performance of present method on viscous solid wall. An incompressible flow is initialed in the computational domain, and the Mach number of the lid is set as $\mathrm{Ma} = 0.1$. The Reynolds number are $\mathrm{Re} = 400, 1000, 3200$, respectively. The computational domain is $[0, 1] \times [0, 1]$, and both the Cartesian and triangular grids are used in the computation. Figure 17 shows the triangular grid used in the case, and the length scale of the triangular grid is $h = 1/16$. The u-velocity profiles along the vertical center-line and the v-velocity profiles along the horizontal center-line are all compared with the reference data in Figs. 18–20. The figures exhibit that the present results match quite well with the data from Ghia [76]. The numerical data extracted from Ref. [22] at $\mathrm{Re} = 1000, 3200$ on 65×65 Cartesian grid are also shown in the figures. It is obvious that the present method can reach the same accuracy with fewer mesh nodes.

G. Blasius incompressible laminar flat plate

The incompressible boundary layer flow over a flat plate is simulated. The Mach number is $\mathrm{Ma}_\infty = 0.15$, and the Reynolds number based on the length of plate is $\mathrm{Re}_\infty = 1 \times 10^5$. The subscript ∞ indicates the state of free stream flow. The length of the flat plate is $L = 100$, and the leading edge of the flat plate is located at $x = 0$. The computational domain is $[-50, 100] \times [0, 100]$. The inflow boundary is applied on the left side of the domain. The upper and right side of the domain is treated as a subsonic outflow boundary. The viscous solid wall is used on the flat plate. The symmetric boundary is implemented at the bottom from the left side to the leading of the plate. It is known to all that using hybrid grid can reduce the grid size obviously, and the hybrid grid is much flexible than structured grid. To show the advantages of hybrid grid, two hybrid grids are considered in the simulation. The coarser grid is shown in Fig. 21, and the details of the two grids are shown in Table III. "Grid 2" has fewer elements than "Grid 1" in the boundary layer.

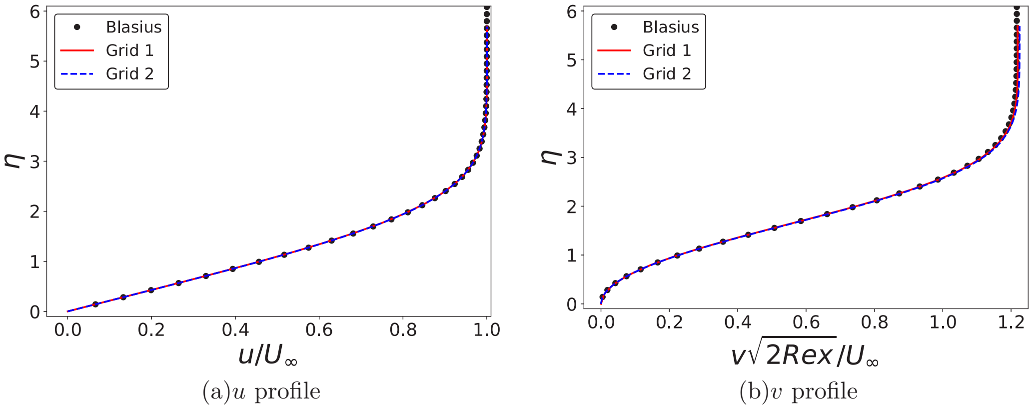

(a)u profile (b)v profile

FIG. 24. Blasius incompressible laminar flat plate: (a) u-velocity and (b) v-velocity profiles at $x/L = 0.5$.

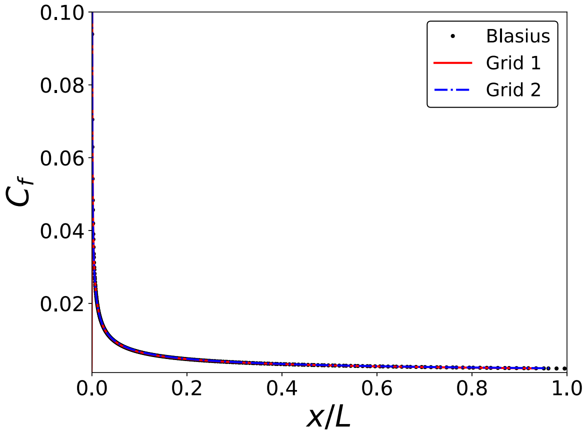

FIG. 25. Blasius incompressible laminar flat plate: The skin friction coefficient distribution along the flat plate.

The velocity profiles versus $\eta = y\sqrt{\frac{U_\infty}{\nu x}}$ are shown in Figs. 22–24. It can be seen clearly in the pictures that the velocity profiles have a good accordance with the Blasius solution at every positions. It is obvious that the present method can approach boundary layer with very few elements. The skin friction coefficient is shown in Fig. 25. The numerical results shows an excellent performance compared with Blasius solution.

H. Taylor-Green vortex at Re = 1600

The Taylor-Green vortex (TGV) is a simple test case for the resolution of the small scales of a turbulent flow by a numerical method. The compressible TGV at Re = 1600 was one of the benchmark problems in the 1st and 2nd International Workshops on High-Order CFD Methods. The reference solution used in the current paper was obtained by Debonis [77] using a high-order dispersion-relation-preserving scheme on a mesh of 512^3 elements. The computational domain is a cubic box of dimensions $[0, 2\pi]^3$, and the periodic boundary is applied on the faces of the cube. In the case, both of the 32^3 and 64^3 grids are used.

The initial condition is set as

$$\begin{aligned} u(t_0) &= u_0 \sin(x/L)\cos(y/L)\cos(z/L),\\ v(t_0) &= -u_0\cos(x/L)\sin(y/L)\cos(z/L),\\ w(t_0) &= 0,\\ p(t_0) &= p_0 + \frac{\rho_0 V_0^2}{16}[\cos(2x/L)\\ &\quad + \cos(2y/L)][\cos(2z/L)+2], \end{aligned} \tag{57}$$

where $\rho_0 = 1$, $p_0 = 100$, $u_0 = 1$, and $L = 1$. The Mach number is set to 0.08, and the initial temperature is 300 K. The volume-averaged kinetic energy and the dissipation rate of the kinetic energy are computed. The volume-averaged kinetic energy is read as

$$E_k = \bar{k} = \frac{1}{\rho_0 \Omega}\int_\Omega \rho \frac{u_i u_i}{2} d\Omega, \tag{58}$$

and the dissipation rate of the kinetic energy is give by

$$\epsilon(E_k) = -\frac{dE_k}{dt}. \tag{59}$$

The numerical results of averaged kinetic energy and the dissipation rate of kinetic energy shown in Fig. 26 are compared with reference data from Debonis [77]. The results have a good accordance with the reference data. The isosurfaces of Q criterions colored by velocity magnitude at times 3, 5, 7, and 9 are shown in Fig. 27. The evolution of flow structure from large-scale vortices to small vortices can be clearly seen in the figure.

IV. CONCLUSION

In the present paper, a high-order numerical scheme is proposed based on the flux reconstruction framework and kinetic inviscid flux. KIF, which aims to find a balance between the advantages of gas-kinetic scheme and lower computational costs, is a combination of TTT scheme and KFVS method. The FR framework is well understood and available. It has the properties of robustness and compactness, which are of great importance for the high-order method. The accuracy order have been verified using the advection of density perturbation problem and isentropic vortex problem. The results show

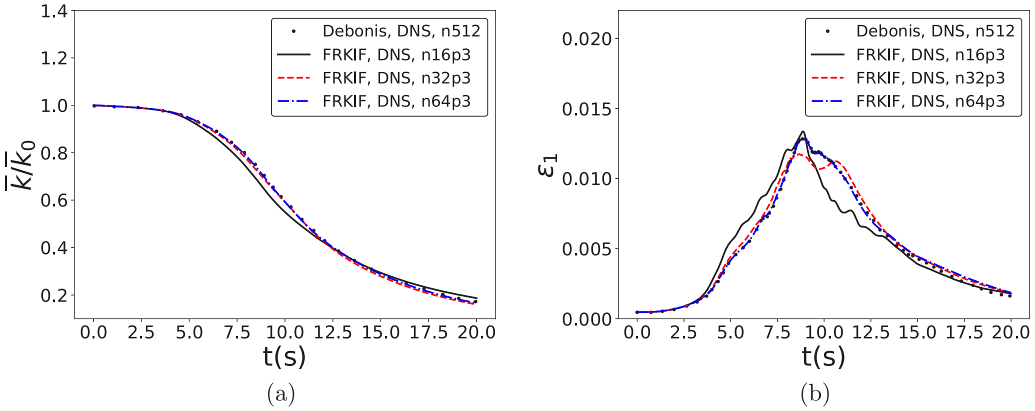

(a) (b)

FIG. 26. The kinetic energy and the dissipation rate: (a) E_k and (b) $\epsilon(E_k)$. nXpY denotes that the grid size is X^3 and the order of polynomial is Y.

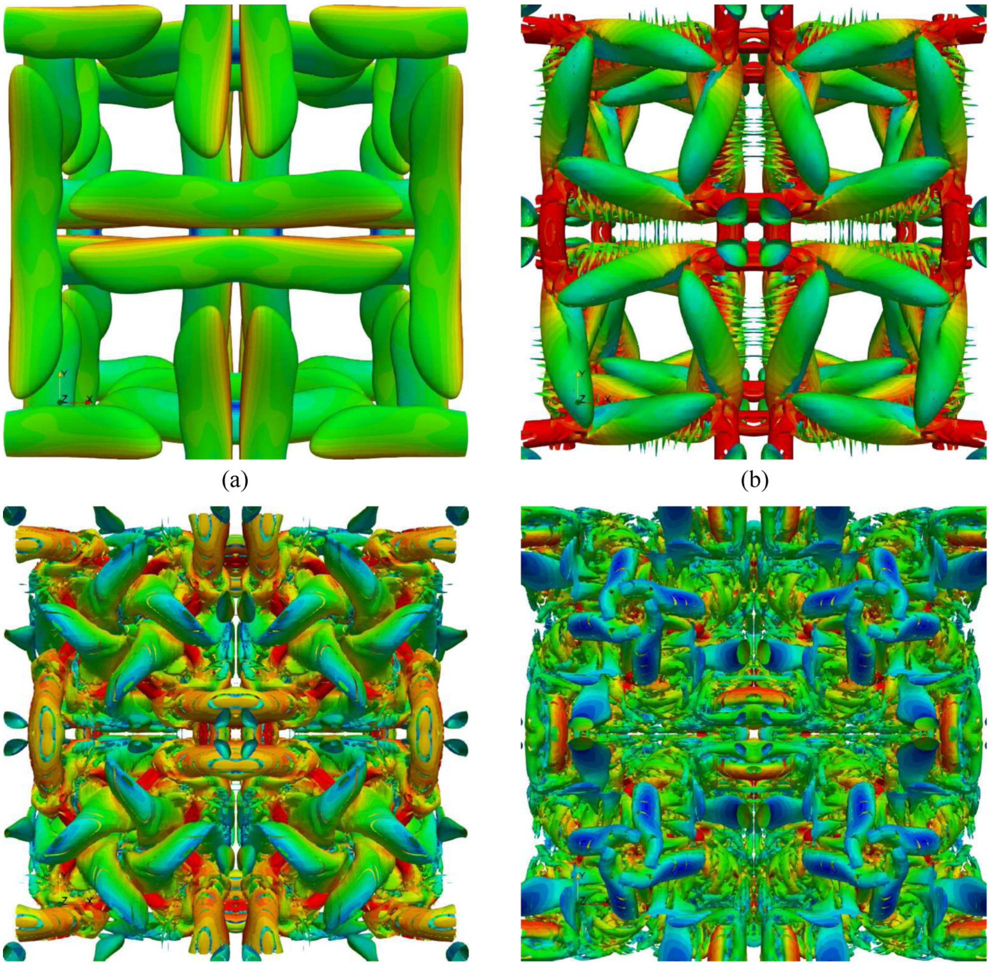
(a) (b) (c) (d)

FIG. 27. Isosurfaces of Q ($Q = 0.5$) criterion colored by velocity magnitude: (a) $t = 3$, (b) $t = 5$, (c) $t = 7$, and (d) $t = 9$.

that the accuracy of present method reaches to the designed order. KIF also can be viewed as an inviscid-viscous splitting version of the gas-kinetic scheme, and the excellent performance of the proposed method can be seen in the simulations of lid-driven cavity flow and Blasius incompressible laminar boundary layer. The good numerical results have shown the success of inviscid-viscous strategy of the gas-kinetic scheme. The Taylor-Green vortex problem has been used to verify the potential of present method to simulate turbulent flow, and excellent results are obtained. The shock capturing technique is used in the simulation of supersonic flow past a circular cylinder. The numerical results have a good accordance with the reference data and the sensor values show that the shock wave is captured quite well.

ACKNOWLEDGMENTS

The present work is supported by National Natural Science Foundation of China (Grants No. 11702223, No. 11902266, and No. 11902264), National Numerical Wind Tunnel Project of China, and 111 Project of China (Grant No. B17037), as well as the ATCFD Project (2015-F-016). The authors appreciate Dongxin Pan for the grid generation used in the simulation of supersonic flow past a circular cylinder.

[1] K. Xu, J. Comput. Phys. **171**, 289 (2001).

[2] K. Xu, M. Mao, and L. Tang, J. Comput. Phys. **203**, 405 (2005).

[3] P. L. Bhatnagar, E. P. Gross, and M. Krook, Phys. Rev. **94**, 511 (1954).

[4] Q. Li, S. Tan, S. Fu, and K. Xu, in *Proceedings of the 13th Asian Congress of Fluid Mechanics* (Engineers Institute of Bangladesh, Dhaka, Bangladesh, 2010), pp. 12–17.

[5] S. Xiong, C. Zhong, C. Zhuo, K. Li, X. Chen, and J. Cao, Int. J. Numer. Methods Fluids **67**, 1833 (2011).

[6] D. Pan, C. Zhong, J. Li, and C. Zhuo, Int. J. Numer. Methods Fluids **82**, 748 (2016).

[7] J. Li, C. Zhong, D. Pan, and C. Zhuo, Comput. Math. Appl. **78**, 1227 (2019).

[8] G. Cao, H. Su, J. Xu, and K. Xu, Aerosp. Sci. Technol. **92**, 958 (2019).

[9] Q. Li, S. Fu, and K. Xu, AIAA J. **43**, 2170 (2005).

[10] H. Liu, K. Xu, T. Zhu, and W. Ye, Comput. Fluids **67**, 115 (2012).

[11] T. Zhu and W. Ye, Numer. Heat Transfer, Part B **57**, 203 (2010).
[12] R. Yuan, C. Zhong, and H. Zhang, J. Comput. Phys. **296**, 184 (2015).
[13] R. Yuan and C. Zhong, Appl. Math. Modell. **55**, 417 (2018).
[14] H. Dong and L. M. Yang, Adv. Appl. Math. Mech. **11**, 1177 (2019).
[15] W. Li, M. Kaneda, and K. Suga, Comput. Fluids **93**, 100 (2014).
[16] J. Li, C. Zhong, Y. Wang, and C. Zhuo, Phys. Rev. E **95**, 053307 (2017).
[17] K. Fujii, Progr. Aerosp. Sci. **41**, 455 (2005).
[18] M. R. Visbal and D. V. Gaitonde, J. Comput. Phys. **181**, 155 (2002).
[19] Q. Li, K. Xu, and S. Fu, J. Comput. Phys. **229**, 6715 (2010).
[20] J. Luo and K. Xu, Sci. China: Technol. Sci. **56**, 2370 (2013).
[21] G. Zhou, K. Xu, and F. Liu, J. Comput. Phys. **339**, 146 (2017).
[22] L. Pan, K. Xu, Q. Li, and J. Li, J. Comput. Phys. **326**, 197 (2016).
[23] L. Pan and K. Xu, Comput. Fluids **119**, 250 (2015).
[24] L. Pan and K. Xu, Commun. Comput. Phys. **18**, 985 (2015).
[25] X. Ji, L. Pan, W. Shyy, and K. Xu, J. Comput. Phys. **372**, 446 (2018).
[26] X. Ji, F. Zhao, W. Shyy, and K. Xu, J. Comput. Phys. **410**, 109367 (2020).
[27] F. Zhao, X. Ji, W. Shyy, and K. Xu, Adv. Aerodyn. **1**, 13 (2019).
[28] S. Liu, J. Cao, and C. Zhong, Phys. Rev. E **102**, 033310 (2020).
[29] T. J. Barth and P. O. Frederickson, AIAA **90**, 0013 (1990).
[30] R. Abgrall, J. Comput. Phys. **114**, 45 (1994).
[31] L. J. Durlofsky, B. Engquist, and S. Osher, J. Comput. Phys. **98**, 64 (1992).
[32] C. F. Ollivier-Gooch, J. Comput. Phys. **133**, 6 (1997).
[33] T. Sonar, Comput. Methods Appl. Mech. Eng. **140**, 157 (1997).
[34] X.-D. Liu, S. Osher, and T. Chan, J. Comput. Phys. **115**, 200 (1994).
[35] C.-W. Shu, in *Advanced Numerical Approximation of Nonlinear Hyperbolic Equations* (Springer, Berlin, 1998), pp. 325–432.
[36] C. Hu and C.-W. Shu, J. Comput. Phys. **150**, 97 (1999).
[37] B. Cockburn and C.-W. Shu, J. Sci. Comput. **16**, 173 (2001).
[38] Y. Liu, W. Zhang, Y. Jiang, and Z. Ye, Comput. Math. Appl. **72**, 1096 (2016).
[39] Q. Wang, Y.-X. Ren, and W. Li, J. Comput. Phys. **314**, 863 (2016).
[40] Q. Wang, Y.-X. Ren, and W. Li, J. Comput. Phys. **314**, 883 (2016).
[41] Q. Wang, Y.-X. Ren, J. Pan, and W. Li, J. Comput. Phys. **337**, 1 (2017).
[42] Z. Wang, Progr. Aerosp. Sci. **43**, 1 (2007).
[43] H. T. Huynh, AIAA **2007**, 4079 (2007).
[44] H. T. Huynh, AIAA **2009**, 403 (2009).
[45] P. E. Vincent, P. Castonguay, and A. Jameson, J. Sci. Comput. **47**, 50 (2011).
[46] A. Jameson, J. Sci. Comput. **45**, 348 (2010).
[47] P. Castonguay, P. E. Vincent, and A. Jameson, J. Sci. Comput. **51**, 224 (2012).
[48] D. A. Kopriva and J. H. Kolias, J. Comput. Phys. **125**, 244 (1996).
[49] D. A. Kopriva, J. Comput. Phys. **128**, 475 (1996).
[50] K. Xu, Numerical hydrodynamics from gas-kinetic theory, Ph.D. thesis, Columbia University, 1993.
[51] D. I. Pullin, J. Comput. Phys. **34**, 231 (1980).
[52] J. C. Mandal and S. M. Deshpande, Comput. Fluids **23**, 447 (1994).
[53] T. Tao and K. Xu, Z. Angew Math. Phys. **50**, 258 (1999).
[54] Y. Sun, C. Shu, L. M. Yang, and C. J. Teo, Adv. Appl. Math. Mech. **8**, 703 (2016).
[55] T. Ohwada, Y. Shibata, T. Kato, and T. Nakamura, J. Comput. Phys. **362**, 131 (2018).
[56] K. Xu, *Direct Modeling for Computational Fluid Dynamics: Construction and Application of Unified Gas-Kinetic Schemes* (World Scientific, Singapore, 2015).
[57] Z. Guo, K. Xu, and R. Wang, Phys. Rev. E **88**, 033305 (2013).
[58] K. Qu, C. Shu, and Y. T. Chew, Phys. Rev. E **75**, 036706 (2007).
[59] K. Xu and J.-C. Huang, J. Comput. Phys. **229**, 7747 (2010).
[60] L. Wu, J. Zhang, J. M. Reese, and Y. Zhang, J. Comput. Phys. **298**, 602 (2015).
[61] C. Liu, Y. Zhu, and K. Xu, J. Comput. Phys. **401**, 108977 (2020).
[62] G.-S. Jiang and C.-W. Shu, J. Comput. Phys. **126**, 202 (1996).
[63] D. Williams, P. Castonguay, P. Vincent, and A. Jameson, J. Comput. Phys. **250**, 53 (2013).
[64] D. M. Williams and A. Jameson, J. Sci. Comput. **59**, 721 (2014).
[65] P.-O. Persson and J. Peraire, AIAA **2006**, 112 (2006).
[66] P.-O. Persson, AIAA **2013**, 3061 (2013).
[67] A. Sheshadri and A. Jameson, AIAA **2014**, 2688 (2014).
[68] M. L. Yu, F. X. Giraldo, M. Peng, and Z. J. Wang, Month. Weath. Rev. **143**, 4823 (2015).
[69] R. Vandenhoeck and A. Lani, Comput. Phys. Commun. **242**, 1 (2019).
[70] M. R. López, A. Sheshadri, J. R. Bull, T. D. Economon, J. Romero, J. E. Watkins, D. M. Williams, F. Palacios, A. Jameson, and D. E. Manosalvas, AIAA **2014**, 3168 (2014).
[71] G. A. Sod, J. Comput. Phys. **27**, 1 (1978).
[72] C.-W. Shu and S. Osher, J. Comput. Phys. **77**, 439 (1988).
[73] M. D. De Tullio, P. De Palma, G. Iaccarino, G. Pascazio, and M. Napolitano, J. Comput. Phys. **225**, 2098 (2007).
[74] V. A. Bashkin, A. V. Vaganov, I. V. Egorov, D. V. Ivanov, and G. A. Ignatova, Fluid Dyn. **37**, 473 (2002).
[75] Q. Li, Y. L. He, and Y. J. Gao, Int. J. Mod. Phys. C **19**, 1581 (2008).
[76] U. Ghia, K. Ghia, and C. Shin, J. Comput. Phys. **48**, 387 (1982).
[77] J. R. DeBonis, AIAA **2013**, 0382 (2013).